Chinese Physics Letters

LETTER

A Novel Rydberg Atom-Based Time Receiving System with Nanosecond-Jitter for eLoran Signals

Cite as: Ziyi Qin *et al*. 2026 *Chin. Phys. Lett.* **43** 090301

Topic Collection: Quantum Frontiers with Rydberg Atoms

DOI CSTR

Recommended Articles

Cavity-Enhanced Rydberg Atom Microwave Receiver
Bang Liu *et al*.
Chin. Phys. Lett. **42**, 053201 (2025)

Sagnac-Enhanced Rydberg Superheterodyne Receiver with Dual-Beam Interference
Hongmei Yan, Taisen Gao, Mingyong Jing, Wenguang Yang, Hao Zhang, Zongkai Liu, Junyao Xie, Liantuan Xiao, Suotang Jia, and Linjie Zhang
Chin. Phys. Lett. **42**, 120601 (2025)

Vortex Dynamics in Binary Ultracold Rydberg Atomic System
Yu Zhong, Dan-Feng Yang, Ya-Xian Liu, Jia Li, Houria Triki, and Qin Zhou
Chin. Phys. Lett. **42**, 080002 (2025)

Nonlinear Spin-Orbit Interaction of Light in a Cold Rydberg Atom Medium
Lu Qin, Chao Hang, Weibin Li, and Xingdong Zhao
Chin. Phys. Lett. **43**, 050303 (2026)

Heterodyne Detection of Low-Frequency Fields via Rydberg EIT with Phase Demodulation
Shenchao Jin, Xiayang Fan, Xin Wang, Yi Song, and Yuan Sun
Chin. Phys. Lett. **42**, 110304 (2025)

A series journal of Chinese Physical Society distributed by IOP Publishing

Chinese Physics Letters

Chin. Phys. Lett. **43** 090301 (2026)

LETTER

DOI: 10.1088/0256-307X/43/9/090301
CSTR: 32039.14.0256-307X.43.9.090301

A Novel Rydberg Atom-Based Time Receiving System with Nanosecond-Jitter for eLoran Signals

Ziyi Qin(覃子意)[1,2,†], Xiaokai Hou(侯晓凯)[1,†], Genwei Cao(曹根伟)[1,2], Chao Xu(徐超)[1], Ying Wang(王莹)[1], Mingtao Cao(曹明涛)[1,*], Ruifang Dong(董瑞芳)[1], Xiaochun Lu(卢晓春)[1], and Shougang Zhang(张首刚)[1]

[1]Key Laboratory of Time and Primary Frequency Metrology and Applications (CAS), National Time Service Center, Chinese Academy of Sciences, Xi'an 710600, China
[2]University of Chinese Academy of Sciences, Beijing 100049, China

[†]These authors contributed equally to this work.
[*]Corresponding author. Email: mingtaocao@ntsc.ac.cn

Rydberg atom-based time-receiving systems enable high-sensitivity demodulation of long-wave signals for precise one-pulse-per-second (1PPS) output, surpassing the limitations of conventional long-wave receivers. Here, we first report the theoretical and experimental demonstration of a nanosecond-jitter Rydberg time-receiving system for eLoran signals. We establish a novel theoretical model that quantitatively reveals the relationship between timing jitter and system parameters, exemplified by the DC Stark shift and the coupling-beam Rabi frequency. Experimentally, we first demonstrate 1PPS timing output based on an atomic system, achieving a root-mean-square (RMS) timing jitter of 27.90 ± 0.39 ns. Furthermore, we demonstrate the timing performance of our system across high-noise conditions and at low input signal amplitudes, validating its robustness under practical weak eLoran signal conditions. This work validates the feasibility of Rydberg atom-based architectures for high-precision ground-based timing and establishes a performance benchmark for next-generation atomic-optical positioning, navigation, and timing (PNT) systems.

Introduction

As the demand for high-precision time synchronization intensifies, a robust positioning, navigation, and timing (PNT) infrastructure has become critical for modern society. Long-wave ground-based time-receiving systems serve as essential backup PNT solutions, offering superior anti-jamming and anti-degradation capabilities through high-power signal transmission. These systems deliver reliable PNT services in challenging environments, including complex electromagnetic scenarios, underground facilities, and indoor spaces [1−6]. However, conventional eLoran receivers face fundamental performance ceilings imposed by electronic thermal noise and environmental interference, limiting further improvements in timing precision.

Recent advances in Rydberg atom-based sensing present a promising approach for overcoming these electronic limitations. The high polarizability of Rydberg atoms enables electromagnetic field detection at sensitivities surpassing conventional electronics by orders of magnitude, making them ideal probes for weak electromagnetic signals [7,8]. Rydberg atom-based electric field measurement originated from the electromagnetically induced transparency (EIT) scheme in a room-temperature rubidium atomic vapor cell [9]. The sensitivity of electric field measurements has been significantly enhanced by several techniques, such as leveraging technical advancements in optical homodyne and frequency modulation spectroscopy [10−13], microwave-dressed Rydberg superheterodyne detection [14−17], microwave-photon conversion [18,19], many-body critical enhancement [20−22], and cavity-enhanced techniques [22,23]. For the electric field shielding effect unique to low-frequency Rydberg sensors, technical routes such as sapphire vapor cells [24], built-in electrode schemes [25,26], heterodyne detection [27], paraffin-coated vapor cells [28], ionization detection [29], and quantum weak measurement [30] have also been adopted. While Rydberg-atom-based sensors have previously been used to receive Loran signals [31,32], to our knowledge, no prior work has yet produced a one-pulse-per-second (1PPS) output or completed the full time service from such signals.

In this work, we bridge this gap by presenting the first experimental realization of an integrated Rydberg time-receiving system designed for long-wave signals, with eLoran waveforms serving as the primary test case. We have constructed a Rydberg-atom-based time-receiving system, consisting of a Rydberg atomic sensor, a timing demodulation module, and a time-to-digital converter (TDC). To bridge atomic-scale response and system-level timing performance, we first develop a theoretical model that quantitatively maps the DC Stark shift and coupling-beam Rabi frequency to timing jitter, thereby establishing a clear optimization pathway. Guided by this framework, we experimentally suppress timing uncertainty by systematically tuning the DC bias voltage and the coupling-beam Rabi frequency to maximize the DC Stark-enhanced signal response. Under optimized conditions, the system achieves a minimum root-mean-square (RMS) timing jitter of 27.90 ± 0.39 ns, which is comparable to that of conventional antenna-based eLoran receivers (32.7 ns [33] and 25.9 ns [34]). Furthermore, we demonstrate robust time-receiving performance across varying noise floors and input signal amplitudes. This work, for the first time, develops a Rydberg-atom-based timing receiver with nanosecond-level timing jitter; it further establishes a theoretical model to analyze how atomic-system parameters affect timing metrics and experimentally verifies the completeness of this model, thereby laying the foundation for next-generation atomic PNT systems.

Experimental Setup

The experimental measurement employs a Rydberg EIT scheme, with the corresponding energy level structure shown in Fig. 1(a), where the probe laser is frequency-locked to the Cesium (Cs) $6S_{1/2}$ $(F = 4) \rightarrow 6P_{3/2}(F' = 5)$ transition while the coupling beam scans the $6P_{3/2}(F' = 5) \rightarrow 59D_{5/2}$ transition with a step size of 189 kHz; upon satisfying the two-photon resonance condition, the EIT spectrum is detected using a silicon photodiode (responsivity 0.6 A/W @ 920 nm, 3 dB bandwidth 20 MHz). In this configuration, the frequency-locked probe and coupling beams counter-propagate within the atomic medium

Received 9 June 2026; accepted 11 August 2026; published 8 September 2026
© 2026 Chinese Physical Society and IOP Publishing Ltd. All rights, including for text and data mining, AI training, and similar technologies, are reserved.

Check for updates

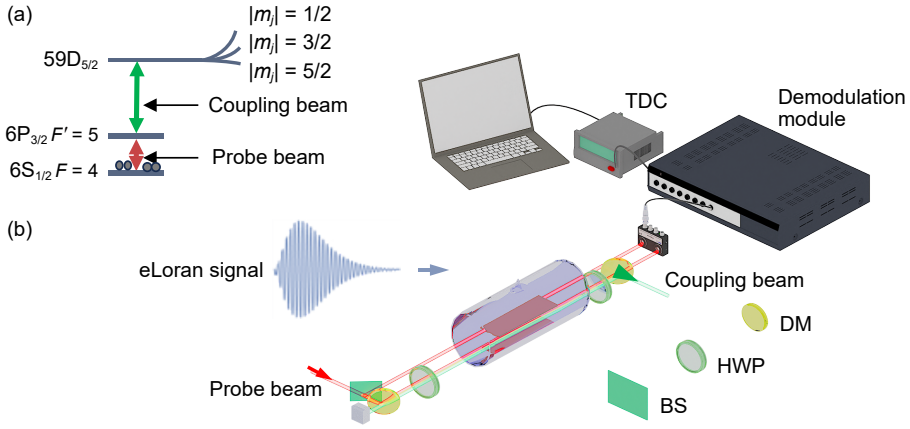

Fig. 1. Energy level and schematic diagram. (a) Energy level of ^{133}Cs atoms for realizing Rydberg EIT. The probe and coupling beams drive the $6S_{1/2}(F = 4) \rightarrow 6P_{3/2}(F' = 5)$ transition and the $6P_{3/2}(F' = 5) \rightarrow 59D_{5/2}$ Rydberg transition, respectively. (b) Experimental setup. The Rydberg time-receiving system comprises a Rydberg sensor, a calibrated eLoran signal source, a timing demodulation module, and a TDC. BS: nonpolarizing beam splitter; RM: reflection mirror; QWP: quarter-wave plate; PBS: polarizing beam splitter; HWP: half-wave plate; DM: dichroic mirror.

to form a transparency window; subsequently, an external eLoran signal induces an AC Stark shift in the Rydberg energy levels, thereby altering the medium's optical properties and modulating the signal onto the EIT peak for demodulation.

Experimentally, the probe beam is provided by an external cavity diode laser with a linewidth of 500 kHz; the coupling beam is generated by frequency-doubling a seed laser after power amplification by a ytterbium-doped fiber amplifier (output power 10 W) through a single pass in a periodically poled lithium niobate (PPLN) crystal (maximum power 500 mW), with a linewidth of 4 kHz. The probe beam has a beam waist of 547.5 μm and a Rabi frequency of $2\pi \times 24.17$ MHz, while the coupling beam possesses a beam waist of 1.0 mm and a Rabi frequency of $2\pi \times 1.25$ MHz. The experimental setup is shown in Fig. 1(b), where the probe and coupling beams are split by a polarizing beam splitter into horizontal and vertical polarization components: the horizontal component is used to construct the modulation transfer spectroscopy frequency stabilization optical path; the transmitted beam, after fiber transmission, serves as the probe light for EIT frequency locking and propagates counter-directionally with the vertically polarized coupling light to form the locked EIT signal, achieving frequency locking of the coupling beam. The full width at half maximum of the locked EIT spectrum is calibrated to 11.7 ± 0.1 MHz via Lorentz fitting, limited by the 3 dB bandwidth of the photodetector. Independently from the locking path, the horizontally polarized probe and coupling beams counter-propagate through the vapor cell to form the measurement EIT spectrum for eLoran signal detection. Before entering the vapor cell, the beams pass through a quarter-wave plate to optimize their polarization states. Simultaneously, a DC bias voltage and the eLoran signal are applied to the vapor cell via a power divider. The transmitted probe beam is then directed to a balanced photodetector using a dichroic mirror, effectively suppressing common-mode noise to achieve high signal-to-noise ratio (SNR) detection.

Additionally, laser power fluctuations cause signal amplitude variations, reducing demodulation and decoding stability; thus, active power stabilization is implemented through an electronically controlled attenuator (dynamic range 0–30 dB, step size 0.01 dB) combined with Proportional-Integral-Derivative (PID) feedback control to dynamically adjust attenuation and achieve closed-loop laser power stabilization. After stabilization, at a sampling branch power of 500 μW, the short-term power fluctuation is less than 0.02% over 30 min, effectively suppressing signal distortion caused by probe laser power fluctuations.

To address signal distortion in eLoran transmission, the experiment employs a room-temperature ^{133}Cs atomic vapor cell (length $L = 100$ mm, cross-sectional diameter $D = 40$ mm) equipped with integrated parallel copper plates (spacing 1.8 ± 0.03 cm). A power divider is used to couple both the bias DC voltage and the eLoran signal into the vapor cell. This configuration generates a DC Stark shift via the applied bias voltage, while the deliberate 0° alignment between the beam polarization and the electric field enables selective addressing of the $m_j = 1/2$ magnetic sublevel. By subsequently locking the coupling beam frequency to the high-slope region of the corresponding EIT resonance, the system effectively suppresses signal distortion induced by the quadratic AC Stark effect.

The eLoran signal fed into the vapor cell is generated by a signal generator (eLoran simulated source, model NTSC_LSG900) that precisely replicates the standard eLoran pulse waveform and spectrum, supporting master/secondary station timing discrimination, chain identification, and simulation of time-difference-of-arrival for multiple stations, thereby emulating complex real-world propagation conditions in the laboratory environment. Following detection, the analog output from the balanced photodetector undergoes bandpass filtering and automatic gain control, and is digitized by an analog-to-digital converter. Subsequently, digital notch and finite impulse response filters are employed to suppress clutter and purify the signal, while precise tracking and locking are achieved via a multi-channel parallel search algorithm. The locked signal is then demodulated, decoded with error correction, and processed for time determination calculation, ultimately outputting a 1PPS signal. In the following, to measure the differential time between the two 1PPS signals, we input both the reference 1PPS (directly output from the eLoran analog source to the timing demodulation module) and the measured 1PPS into a TDC featuring an 8 ps time resolution. Finally, the RMS of these time differences is calculated as the quantitative metric for timing jitter.

Results and Discussions

To verify the feasibility of optimizing the system timing jitter of a Rydberg sensor by improving its SNR, as predicted in the theoretical model, we characterize the SNR and envelope cycle difference (ECD) of the Rydberg sensor under varying input signal amplitudes. Principally, the SNR of the Rydberg sensor is the core metric that directly governs the magnitude of system timing jitter: a higher SNR corresponds to more stable timing detection capability and a lower achievable jitter floor. The ECD is defined as the time interval between the 30-μs point on the eLoran pulse envelope and the third positive zero-crossing of its carrier; it is the key indicator for pulse demodulation performance. The absolute value of the ECD directly determines whether the system can correctly demodulate the eLoran signal and stably output a 1PPS signal, with a smaller absolute ECD value indicating higher demodulation accuracy and reliability.

Measurements were conducted over 2000-second cycles with input amplitudes varying from 90 to 65 dB·μV (in 5 dB·μV steps) at a fixed noise level of 60 dB·μV, using a probe power of 10 μW, a coupling power of 45 mW, and a 510-mV DC offset (corresponding to

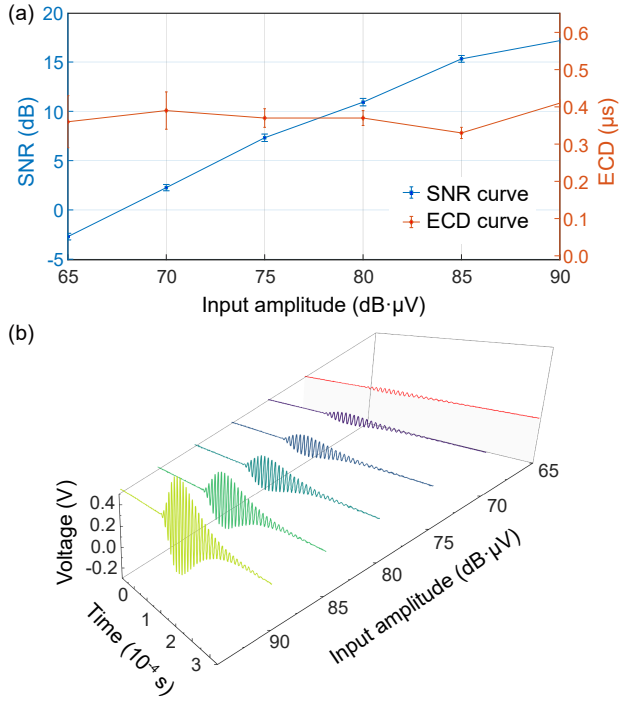

Fig. 2. Effect of the input signal amplitude on the receiver performance. (a) Measured SNR (left axis) and ECD (right axis) as functions of the input amplitude over the range 65–90 dB·μV. (b) Time-domain waveforms at the photodetector output for the same set of input amplitudes (65–90 dB·μV); the eLoran pulse envelope becomes progressively more distinguishable from the background noise as the input amplitude increases, consistent with the rising SNR in (a).

$\Delta_{DC} = 6.8$ MHz). The SNR was derived from EIT amplitude spectra by comparing the background noise and the signal peak power at 100 kHz, while the ECD was measured via digital phase detection, extracting the time difference between the envelope and the pulse zero-crossings. Results [as shown in Fig. 2(a)] indicate that the SNR monotonically increases (blue curve) and the ECD remains stable (orange curve), revealing improved signal quality and stabilized ECD with higher input amplitude. The SNR (blue curve, left axis) exhibits a monotonic increase from -2.71 ± 0.34 dB at 65 dB·μV to 15.32 ± 0.30 dB at 90 dB·μV, demonstrating a near-linear relationship over the measured range. This trend indicates that the Rydberg sensor maintains consistent responsivity across the tested dynamic range without saturation effects. The Rydberg system maintains the ECD within 0.33–0.40 μs regardless of input amplitude. This behavior stems from the quantum-coherent nature of EIT detection, which responds to the electric field amplitude rather than to power, thereby preserving phase relationships even under marginal SNR conditions. Results in Fig. 2(b) demonstrate time-domain waveforms at the photodetector output for the same set of input amplitudes (65–90 dB·μV); the eLoran pulse envelope becomes progressively more distinguishable from the background noise as the input amplitude increases, consistent with the rising SNR in Fig. 2(a).

Based on the above experimental results, two core conclusions are drawn as follows. First, the operational ranges of both SNR and ECD consistently satisfy the stringent thresholds required for robust eLoran demodulation and stable 1PPS generation, according to the known standard [35]. Second, the near-linear response between the SNR variation of our Rydberg sensor and that of the external input signal enables optimization of the Rydberg sensor's intrinsic SNR to deliver a practical and linear improvement in timing performance for weak signals or high-noise scenarios.

In long-wave time receiving systems, minimizing timing jitter is fundamental to achieving stable and precise 1PPS output. Enhancing timing stability directly dictates the operational reliability of resilient

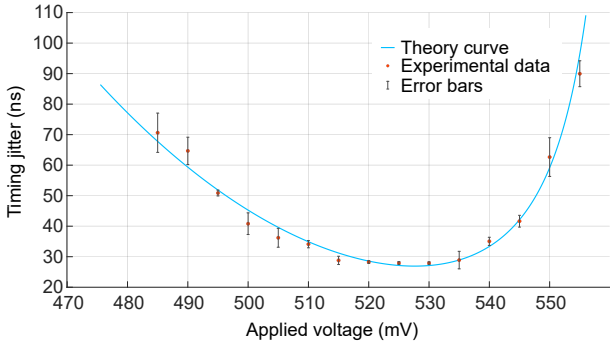

Fig. 3. Optimizing timing jitter under varying applied DC voltage. The blue curve is the theoretical curve; the orange dots are experimental results obtained when the input amplitude is set at 80 dB·μV and the noise amplitude is set at 50 dB·μV. The coupling power is fixed at 50 mW.

PNT infrastructure, particularly in complex electromagnetic environments. According to our theoretical model, the timing jitter is fundamentally constrained by the sensing SNR. Consequently, maximizing the SNR serves as the primary physical pathway to suppress jitter, establishing a quantifiable optimization target for Rydberg long-wave time receiving system. Experimentally, this SNR enhancement is realized by precisely tuning the DC bias voltage applied to the vapor cell electrodes, which induces a controlled quadratic Stark shift to align the maximum slope of the $m_j = 1/2$ state EIT resonance with the coupling beam locking frequency. This optimal spectral alignment maximizes the optical transduction efficiency of the atomic antenna, thereby directly enhancing the effective SNR and systematically driving the timing jitter toward its theoretical minimum.

To experimentally validate the suppression of timing jitter via DC bias voltage tuning, the input amplitude of the eLoran signal was fixed at 80 dB·μV, with broadband white noise at 50 dB·μV superimposed to emulate realistic electromagnetic interference. Each independent measurement cycle was conducted over an integration time of 2000 s, with the DC bias voltage stepped in 5 mV increments across the 480–560 mV range. After correlation capture and phase tracking of the sensed eLoran signal, the demodulated signal generated a 1PPS pulse that was sent to the TDC, which recorded the differential time between this measured 1PPS and the reference 1PPS.

Results (as in Fig. 3) show agreement between the theoretical curve [blue solid line, derived from the theoretical model in Supplementary Materials (SM)] and experimental timing jitter (orange dots). The minimum timing jitter of 27.90 ± 0.39 ns occurred at 525 mV DC bias. At bias voltages below 485 mV and above 555 mV, where timing instability exceeded 90 ns, the SNR fell below the threshold for correlation locking, preventing reliable demodulation and 1PPS output. The experimentally observed trend of timing jitter closely follows the slope variation of the EIT transmission profile, which approximates a Lorentzian lineshape. In the spectral region extending from the resonance wing to the point of maximum dispersion slope, the slope evolves gradually; consequently, under equal-step DC bias voltage increments that induce proportional Stark frequency shifts, the enhancement in detection sensitivity proceeds slowly, resulting in a relatively gradual reduction of timing jitter. This behavior corresponds to the experimental results in the 485–525 mV bias range. Conversely, in the frequency region from the maximum-slope point toward the EIT resonance center, the slope changes more rapidly, leading to an accelerated increase in timing jitter as the locking point deviates from the optimal alignment. These results collectively reveal that, in a Rydberg long-wave time receiving system equipped with integrated parallel electrodes, there exists a minimum in timing jitter as a function of the DC bias voltage. This observation experimentally validates the effectiveness of our theoretical strategy for jitter suppression via DC-Stark compensation.

The other critical parameter influencing timing jitter is the Rabi frequency, as it directly governs the SNR by controlling the EIT

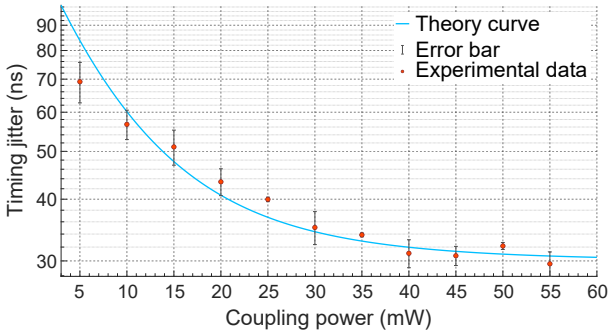

Fig. 4. Optimizing timing jitter on varying coupling power. The blue curve is the theoretical curve; the orange dots are experimental results obtained when the input amplitude is set at 80 dB·μV and the noise amplitude is set at 50 dB·μV. The applied DC voltage is fixed at 525 mV.

linewidth $\Gamma = \Omega_c^2/\gamma_{rg} + \gamma_{eg}$ and probe absorptance. Variations in the EIT peak slope result in SNR changes, which subsequently alter timing jitter. In optical Rydberg systems, laser intensity noise, atomic density fluctuations, and Doppler broadening degrade Rabi frequency stability: intensity noise causes random fluctuations in Ω_c through laser power variations; density fluctuations modify the interaction strength in light–atom interactions; and Doppler broadening dictates the Ω_c magnitude required to achieve a target EIT linewidth in thermal vapor, necessitating higher Rabi frequencies for larger Doppler widths.

Given the proportionality $\Omega_c \propto \sqrt{P_c}$, we optimized timing jitter by tuning the coupling power from 5 mW to 55 mW in 5 mW steps, while maintaining the DC bias at the optimal 525 mV, the probe power at 10 μW, and the signal amplitude at 80 dB·μV. Figure 4 shows the dependence of timing jitter σ_e on coupling power, with the blue solid line representing the theoretical prediction (derived from the theoretical model in the SM) and the orange data points indicating experimental measurements. The measured σ_e decreases as power increases, with a rapid decline in the low-power regime (5–30 mW) and a gradual plateau beyond 40 mW. For $P_c \geq 40$ mW, variations in σ_e with Rabi frequency fall within experimental error bars, indicating the optimal operating range for timing jitter, improving timing jitter from 69.17 ± 6.50 ns at 5 mW to 29.59 ± 1.68 ns at 55 mW. The results demonstrate that within the experimental power range, enhancing the Rabi frequency by adjusting the coupling power effectively improves the SNR of Rydberg signal measurements. This approach provides another effective pathway for optimizing the timing performance of Rydberg-based time receiving systems, complementing the DC compensation strategy for comprehensive stability enhancement.

The optimization of timing jitter via DC voltage and coupling power enhances the timing performance of the system under controlled conditions. However, in real-world electromagnetic environments, strong noise or weak signals can directly degrade SNR of the sensor, thereby compromising timing performance. Therefore, systematically characterizing the timing jitter of the Rydberg receiver under degraded SNR conditions is essential to map its operational boundaries and rigorously validate its robustness prior to practical deployment in complex electromagnetic environments.

We set the measurement duration to 2000 s, with the coupling power fixed at 20 mW and the DC voltage at 525 mV. First, the signal power was held constant at 80 dB·μV while varying the noise amplitude input to the vapor cell from the eLoran source: from 60 dB·μV to 80 dB·μV in 5 dB·μV steps, then from 80 dB·μV to 90 dB·μV in 1 dB·μV steps for finer resolution near the degradation threshold. This approach systematically characterizes noise resilience under controlled conditions. Figure 5(a) (Orange dots with error bars) illustrates the relationship between noise amplitude and timing jitter. Timing jitter remains steady at 41.58–43.77 ns when the noise amplitude is below 75 dB·μV (corresponding to an input signal SNR of 5 dB), but increase exponentially beyond this threshold, reaching approximately 81.90 ns at 90 dB·μV (corresponding to an input signal SNR of −10 dB). Figure 5(b) using orange squares in the legend for timing jitter, demonstrates how signal amplitude affects timing jitter: timing jitter improves from 84.58 ns to 41.35 ns as the signal amplitude increases from 65 dB·μV to 80 dB·μV, and further improvement slows down beyond 74 dB·μV, reaching optimized timing jitter of 41.35 ns for input amplitudes of 80 dB·μV (corresponding to an input SNR of 10 dB). The results demonstrate the applicability of our system under high-noise and weak-signal conditions. With further improvements in noise resilience and sensitivity to weak signals, such as squeezed-light injection or cascade EIT schemes, such systems can enable practical timing applications in real-world electromagnetic environments.

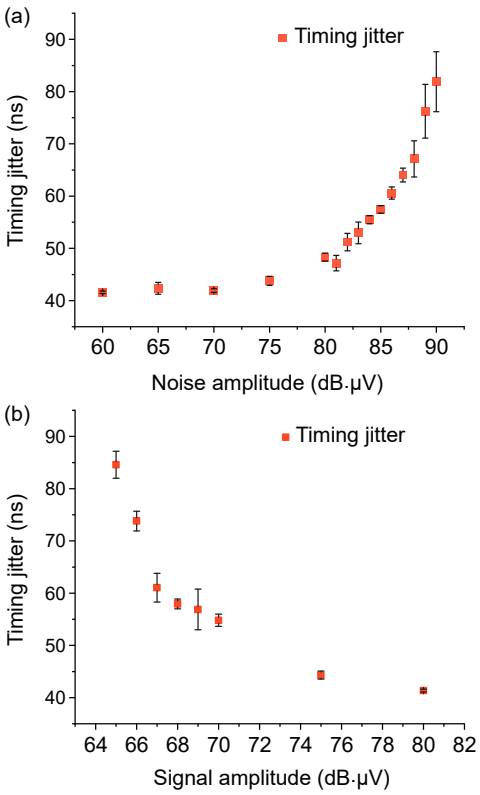

Fig. 5. Timing jitter under degraded input SNR conditions. (a) Orange dots are experimental timing jitter under varying noise amplitude (input signal amplitude fixed at 80 dB·μV). (b) Orange squares are experimental timing jitter under varying signal amplitude (input noise amplitude fixed at 70 dB·μV).

Conclusion

In conclusion, we demonstrate a Rydberg-atom-based long-wave time receiving system capable of reliable 1PPS timing output, and establish a theoretical model for the systematic optimization of system parameters to improve its timing performance. Theoretical modeling reveals that optimal performance requires DC voltage tuning for DC Stark shift compensation to align the locking frequency with the maximum dispersion slope of the EIT resonance and coupling laser power adjustment to balance optical transmittance with technical noise via Rabi frequency control. Experimental validation demonstrates that these optimization approaches yield agreement with theoretical predictions: a timing jitter minimum of 27.90 ± 0.39 ns at 525 mV DC voltage, while optimizing coupling power from 5 mW to 55 mW improves stability from 69.17 ± 6.50 ns to 29.59 ± 1.68 ns. Crucially, the system maintains stable 1PPS timing output even under challenging conditions where the input signal SNR drops below −10 dB or signal levels decrease to 65 dB·μV. This work establishes the first theoretical model for timing jitter in a Rydberg long-wave time receiving

system, validates system performance in high-noise and weak-signal environments, and provides effective methodologies for enhancing timing stability. In the future, timing performance will be further optimized by improving the frequency stabilization system and the timing synchronization among system components, so as to facilitate practical, field-deployable Rydberg timing applications.

Acknowledgements

This work was supported by the Youth Innovation Promotion Association of the Chinese Academy of Sciences (Grant Nos. 2021408, 2022413, and 2023425) and the Shaanxi Provincial Technical Innovation Guidance Special Fund (Grant No. 2024QY-SZX-19).

References

[1] Gao W M 2019 *Inf. Commun.* **7** 166 (in Chinese)
[2] Zhang H Y, Xu B, Li H B, Liao D Y, and Chen H Q 2020 *J. Astronaut. Metrol. Meas.* **40** 6 (in Chinese)
[3] Wang D D, Xi L X, Pu Y R, Liu J F, and Zhou L L 2015 *IEEE Antennas Wirel. Propag. Lett.* **15** 734
[4] Fang T H, Kim Y, Park S G, Seo K, and Park S H 2020 *Int. J. Control Autom. Syst.* **18** 2349
[5] Son P W, Park S G, Han Y, and Seo K 2020 *IEEE Access* **8** 193708
[6] Li S F, Wang Y L, Hua Y, and Xu Y L 2012 *Chin. J. Sci. Instrum.* **33** 1407 (in Chinese)
[7] Schlossberger N, Prajapati N, Berweger S, Rotunno A P, Artusio-Glimpse A B, Simons M T, Sheikh A A, Norrgard E B, Eckel S P, and Holloway C L 2024 *Nat. Rev. Phys.* **6** 606
[8] Zhang H, Ma Y, Liao K Y, Yang W G, Liu Z K, Ding D S, Yan H, Li W H, and Zhang L J 2024 *Sci. Bull.* **69** 1515
[9] Sedlacek J A, Schwettmann A, Kübler H, Löw R, Pfau T, and Shaffer J P 2012 *Nat. Phys.* **8** 819
[10] Kumar S, Fan H Q, Kübler H, Sheng J T, and Shaffer J P 2017 *Sci. Rep.* **7** 42981
[11] Kumar S, Fan H Q, Kübler H, Jahangiri A J, and Shaffer J P 2017 *Opt. Express* **25** 8625
[12] Shaffer J P and Kübler H 2018 *Proc. SPIE* **10674** 106740C
[13] Fan H Q, Kumar S, Sedlacek J, Kübler H, Karimkashi S, and Shaffer J P 2015 *J. Phys. B: At. Mol. Opt. Phys.* **48** 202001
[14] Jing M Y, Hu Y, Ma J, Zhang H, Zhang L J, Xiao L T, and Jia S T 2020 *Nat. Phys.* **16** 911
[15] Gordon J A, Simons M T, Haddab A H, and Holloway C L 2019 *AIP Adv.* **9** 045030
[16] Cai M, Xu Z, You S, and Liu H 2022 *Photonics* **9** 250
[17] Holloway C L, Prajapati N, Artusio-Glimpse A B, Berweger S, Simons M T, Kasahara Y, Alù A, and Ziolkowski R W 2022 *Appl. Phys. Lett.* **120** 204001
[18] Borówka S, Pylypenko U, Mazelanik M, and Parniak M 2024 *Nat. Photon.* **18** 32
[19] Tu H T, Liao K Y, Zhang Z X, Liu X H, Zheng S Y, Yang S Z, Zhang X D, Yan H, and Zhu S L 2022 *Nat. Photon.* **16** 291
[20] Ding D S, Liu Z K, Shi B S, Guo G C, Mølmer K, and Adams C S 2022 *Nat. Phys.* **18** 1447
[21] Wang Y J, Zhang J, Zhang Z Y, Shao S Y, Li Q, Chen H C, Ma Y, Han T Y, Wang Q F, Nan J D, Yin Y M, Zhu D Y, Fang Q Q, Yu C, Liu X, Guo G C, Liu B, Zhang L H, Ding D S, and Shi B S 2020 *Nat. Commun.* **11** 177
[22] Wang Q X, Liang Y K, Wang Z H, Guan S J, Yang P F, Zhang P F, Li G, and Zhang T C 2025 *Sci. China Phys. Mech. Astron.* **68** 264211
[23] Liang Y K, Wang Q X, Wang Z H, Guan S J, Yang P F, Zhang Y C, He J, Zhang P F, Li G, and Zhang T C 2025 *Opt. Express* **33** 13034
[24] Jau Y Y and Carter T 2020 *Phys. Rev. Appl.* **13** 054034
[25] Li L, Jiao Y C, Hu J L, Li H Q, Shi M, Zhao J M, and Jia S T 2023 *Opt. Express* **31** 29228
[26] Lei M W and Shi M 2024 *Opt. Lett.* **49** 5547
[27] Jin S C, Fan X Y, Wang X, Song Y, and Sun Y 2025 *Chin. Phys. Lett.* **42** 110304
[28] Chandra A, Paensin N, and Dumke R 2026 arXiv: 2603.13827 [quant-ph]
[29] Glick J, Dickson J R, Wood J, and Kunz P 2026 arXiv: 2604.01513 [physics.atom-ph]
[30] Wang D, Jin S C, Fan X Y, Li H J, Liu J T, Huang J Z, Zeng G H, and Sun Y 2026 arXiv: 2603.09518 [physics.atom-ph]
[31] Xie Y P, Lei M W, and Shi M 2026 *Acta Phys. Sin.* **75** 030602
[32] Qin Z Y, Hou X K, Cao G W, Xu C, Wang Y, Cao M T, Dong R F, Lu X C, and Zhang S G 2026 *Acta Phys. Sin.* **75** 170301
[33] Li Y, Hua Y, Yan B R, and Guo W 2020 *Sensors* **20** 6518
[34] Yin K X, Wu J F, Ning R Z, Chen Y Q, Liu Q, and Wang K 2025 *Electronics* **14** 789
[35] Maxim L D and Knudsen V L 1992 Loran-C User Handbook COMDTPUB P16562.6 (Washington, DC: United States Coast Guard)